for details see (*22*)], with gradient corrections for the exchange-correlation functional (*23*). The Kohn-Sham equations were solved in conjunction with norm-conserving nonlocal pseudopotentials for the valence electrons (*24*) and a plane-wave basis (i.e., no atom-centered basis functions were used) with a high kinetic energy cutoff of 845 eV; a calculation for the 4-bp duplex d(GAGG) with 48 $H_2O$ and 6 Na makes for 1240 valence electrons. The algorithm for solving the density-functional Kohn-Sham equations uses a Fermi distribution function for the electrons, which is a very effective way of dealing with degenerate or near-degenerate energy levels [see (*22*)]. The Fermi temperature that we used is rather low (0.01 eV/$k_B$), which assures that the Fermi function is operative only on the near-degenerate levels at the top of the level spectrum and not anywhere else (where the spectral gaps are larger). The BO-LSD-MD method is particularly suitable for calculations of charged systems because no periodic replication of the ions is imposed [that is, no supercells are used; see (*22*)]. To illustrate the accuracy of the calculations, we give the vertical (v) and adiabatic (a) ionization potentials (IP), calculated for the isolated nucleobases as the total energy difference between the neutral and ionized species. For T, vIP = 8.73 eV, aIP = 8.54 eV; for C, vIP = 8.54 eV, aIP = 8.43 eV; for A, vIP = 8.11 eV, aIP = 7.96 eV; for G, vIP = 7.70 eV, aIP = 7.20 eV. The values obtained from our calculations are consistently lower by 3 to 6% than the measured values (*16*, *25*, *26*).

22. R. N. Barnett, U. Landman, *Phys. Rev. B* **48**, 2081 (1993).
23. P. P. Perdew *et al.*, *Phys. Rev. Lett.* **77**, 3865 (1996).
24. N. Troullier, J. J. Martins, *Phys. Rev. B.* **43**, 1993 (1991).
25. V. M. Orlov, A. N. Smirnov, Y. M. Varshvsky, *Tetrahedron Lett.* **48**, 4377 (1976).
26. S. G. Lias, *et al.*, *J. Phys. Chem. Ref. Data* **17** (suppl. 1), 1 (1988).
27. The classical molecular dynamics simulations were performed using the AMBER95 force field with the NWChem package (*28*). The computational cell contained the 7-bp duplex d(5′-AGAGGAG-3′) (Fig. 1A), which was kept (except for the hydrogens) in its crystallographic structure (*29*), as well as 12 $Na^+$ and 840 $H_2O$, which, together with the DNA hydrogen atoms, were treated dynamically. The dimensions of the Cartesian computational cell were 32 Å by 32 Å by 37 Å, with the larger dimension parallel to the DNA helix axis. The duplex was terminated on both ends by removing the DNA double helix beyond the nearest neighboring P atoms and substituting a hydrogen atom for the removed part. A time step of 1 fs was used throughout, using the velocity Verlet algorithm. The system was equilibrated first at a temperature of 300 K for 200 ps, and phase-space trajectories accumulated for the subsequent 1.4 ns were used in the analysis reported here.
28. High Performance Computational Chemistry Group, *NWChem, A Computational Chemistry Package for Parallel Computers, version 4.0.1*, (Pacific Northwest National Laboratory, Richland, WA, 1998).
29. S. Arnott *et al*., in *Handbook of Biochemistry and Molecular Biology*, G. D. Fasman, Ed. (CRC Press, Cleveland, 1977), pp. 411–422.
30. Supplementary material is available at *Science* Online at www.sciencemag.org/cgi/content/full/294/5542/567/DC1.
31. L. McFail-Isom, C. C. Sines, L. L. Williams, *Curr. Opin. Struct. Biol.* **9**, 298 (1999).
32. R. Marcus, *J. Phys. Chem. B.* **102**, 10071 (1998)
33. The configurations used in the quantum calculations were extracted from the classical MD simulations. In each case, the configuration was re-optimized to the nearest local potential energy minimum through the use of damped MD. The main effect of this process was to rearrange some of the hydrogen bonds of the outer hydration shell of the selected configuration, and the effect of thermal disorder is maintained. We have verified for a 2-bp duplex d(5′-GG-3′) that quantum mechanical relaxation including the DNA bases, the sugar-phosphate groups, counterions, and water solvation, starting from optimized configurations, do not alter the results in any substantial way.
34. Comparative calculations on a 2-bp duplex d(5′-GG-3′), with sugar-phosphates, counterions and water solvation, have shown that inclusion of water molecules beyond those considered here does not modify the quantum mechanical results in any substantial manner.
35. The higher vIP of the hydrated configuration may, at first, seem surprising in light of the common notion that hydration serves to screen electrostatic interactions and, thus, reduce the effect of the counterions and negatively charged phosphates, whereas the opposite is found here. However, the above screening notion is anchored in bulk (often coarse-grained) considerations, and it does not apply to the interfacial interactions and molecular length scale that characterize the hydration process of DNA. Underlying the increase of the vIP in the hydrated system (that is, stronger binding of the electrons), as well as the marked effect of hydration on the spatial distribution of the hole (compare Fig. 3, A and B), is the preferential orientational ordering of the water molecules in the first (and to a smaller extent in the second) hydration shell, with the enhanced binding originating from the added attractive interaction between the electrons and the dipolar charge distribution of the water molecules.
36. In configuration (I) of the neutral duplex, four orbitals at the top of the occupied electronic manifold form a group separated from the rest of the occupied orbitals by a mini gap (0.52 eV ). We denote these orbitals as $\Psi_1$ (−4.162 eV ), $\Psi_2$ (−4.392 eV), $\Psi 3$ (−4.426 eV), and $\Psi_4$ (−4.798 eV), in descending order of their energies (with the orbital energies given in parenthesis; i.e., $\Psi_1$ shown in Fig. 2A is the HOMO). $\Psi_1$ and $\Psi_2$ are localized on the $G_3G_4$ pair, $\Psi_3$ on $G_1$, and $\Psi_4$ on $A_2$. After ionization, the whole spectrum shifts to lower energies and the above four orbitals mix with each other. The two highest occupied spin-orbitals of the radical cation (shown in Figs. 2C and 2D) are nearly degenerate (with energies of −6.688 eV and −6.703 eV, respectively) and they are delocalized over the 4 base pairs. The occupancies of these spin-orbitals by the lone electron of the ionized duplex are 0.64 and 0.36, respectively. Alternatively, these spin-orbitals may be regarded as the "hole-orbitals" with hole occupancies of 0.36 and 0.64, respectively.
37. J. Tchou *et al.*, *Proc. Natl. Acad. Sci. U.S.A.* **88**, 4690 (1991).
38. Preliminary results from our laboratory show that exchange of $Na^+$ for $K^+$ or $Li^+$ has no measurable effect on the efficiency of charge migration.
39. Supported by the National Science Foundation, the Department of Energy, and the Air Force Office of Scientific Research. Computations were performed on an IBM SP2 computer at the Georgia Tech Center for Computational Material Science and at NERSC, Berkeley, CA.

25 May 2001; accepted 10 September 2001

# Reproducible Measurement of Single-Molecule Conductivity

**X. D. Cui,[1] A. Primak,[2,3] X. Zarate,[2] J. Tomfohr,[1] O. F. Sankey,[1] A. L. Moore,[2] T. A. Moore,[2] D. Gust,[2] G. Harris,[3] S. M. Lindsay[1]**

**A reliable method has been developed for making through-bond electrical contacts to molecules. Current-voltage curves are quantized as integer multiples of one fundamental curve, an observation used to identify single-molecule contacts. The resistance of a single octanedithiol molecule was 900 ± 50 megohms, based on measurements on more than 1000 single molecules. In contrast, nonbonded contacts to octanethiol monolayers were at least four orders of magnitude more resistive, less reproducible, and had a different voltage dependence, demonstrating that the measurement of intrinsic molecular properties requires chemically bonded contacts.**

Wiring a single molecule into an electrical circuit by chemically bonding each end to a metal conductor is a key requirement for molecule-based electronics. Although conceptually simple, this goal has proven elusive. The variety of methods for contacting molecules includes bonding dithiolated molecules into break junctions (*1*), dipping nanotubes into a mercury pool (*2*), touching molecules in an insulating matrix with a conducting atomic force microscope (AFM) (*3*), using a scanning tunneling microscope (STM) to connect to gold particles attached to dithiolated monolayers (*4*, *5*), and contacting two monolayers together with a mercury-drop electrode (*6*). These pioneering experiments have demonstrated that unambiguous contact to a single molecule is difficult to achieve, as shown by large disparities in conductivities reported for identical (*7*, *8*) or similar (*1*, *9*) molecules. Measured currents can be very sensitive to applied stress (*3*, *10*, *11*), and calculated conductivity can disagree with experimental results by several orders of magnitude (*12*). In many cases, electrical connections to the molecules have been made via nonbonded mechanical contacts rather than chemical bonds, and it is likely that this may account for some of the discrepancies.

Here we report a reliable method for chemically bonding metal contacts to either end of an isolated molecule and measuring the current-voltage $I(V)$ characteristics of the resulting circuit. Molecules of 1,8-octanedithiol were inserted into an octanethiol monolayer [on Au(111)] using a replacement reaction (*13*) whereby one of the two thiol groups becomes chemically bound to the gold substrate (*14*–*17*). The octanethiol monolayer

[1]Department of Physics and Astronomy, [2]Department of Chemistry and Biochemistry, Arizona State University, Tempe, AZ 85287, USA. [3]Motorola, 2100 East Elliot Road, AZ34/EL 704, Tempe, AZ 85284, USA.

acts as a molecular insulator, isolating the dithiol molecules from one another. The thiol groups at the top of the film were derivatized by incubating the monolayer with a suspension of gold nanoparticles (*17*). A gold-coated conducting AFM probe was used to locate and contact individual particles bonded to the monolayer (Fig. 1A).

$I(V)$ measurements made on over 4000 nanoparticles produced only five distinct families of curves. Representative curves from each family are shown in Fig. 1B. The curves correspond to multiples of a fundamental curve, lying on this fundamental curve when divided by the appropriate integer (Fig. 1C). To test for this property in all of the measured curves, we found values of a continuous divisor, $X$, that minimized the variance between the fundamental data set and all others. A histogram of 4600 values of $X$ (Fig. 1D) shows that it is sharply peaked at the integer values 1, 2, 3, 4, and 5 (with a negligible number of higher values not shown). The fundamental set, containing more than 1000 curves, is ascribed to assemblies in which a single dithiol molecule links the gold nanoparticle to the underlying gold substrate.

The $I(V)$ characteristics of the dithiol molecules bound to the gold nanoparticles differ dramatically from those of alkanethiols that are contacted through nonbonded interactions with the AFM tip. Figure 2A shows a measured $I(V)$ curve for a bonded contact to a single dithiol molecule (current is on a log scale). An $I(V)$ curve measured with a nonbonded contact to the octanethiol monolayer is also shown. The current through the bonded contact is not only much larger but also has a very different voltage dependence. For nonbonded contacts, the experimentally observed $I(V)$ characteristics are dominated by the contact rather than by intrinsic molecular properties. In the ohmic region (between $\pm$0.1 V) the single molecule has a resistance of 900 ($\pm$50) megohm. In the same voltage range, measurement of the resistance of the nonbonded contact is limited by noise, but the resistance is at least $10^4$ gigohm (at a contact stress of 1 GPa).

A theoretical single-molecule $I(V)$ curve was calculated with scattering theory (*18–20*) carried out self-consistently so as to avoid the need for fitting parameters such as the energy difference between the metallic Fermi energy and a molecular orbital. The results of this calculation are shown on a log scale in Fig. 2A. The shapes of the calculated and measured curves are in agreement, and the absolute values of current agree to within a factor of 6. This represents a remarkable improvement relative to previous comparisons of calculated and measured molecular conductivity [for example, a factor of 500 (*12*)]. Simulations were also carried out for a nonbonded monothiol with the terminal methyl group positioned near a gold surface. The results were similar to the dithiol simulation, rather than the measured curve (Fig. 2A), but depend strongly on the exact placement of the methyl group with respect to the gold. This placement is difficult to determine theoretically in the absence of bond formation.

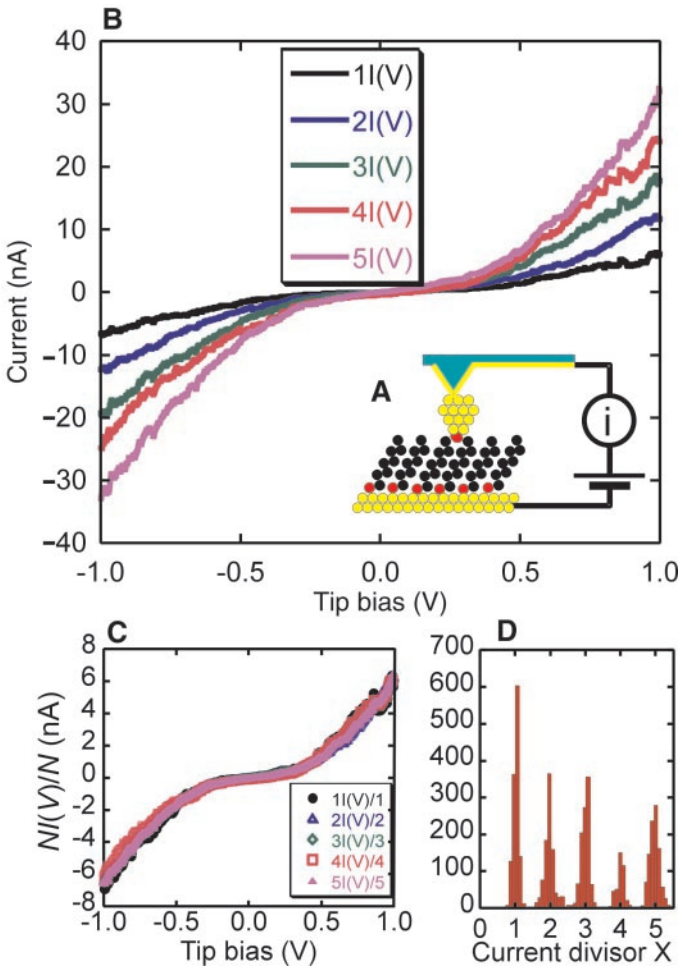


**Fig. 1.** (**A**) Schematic representation of the experiment. The sulfur atoms (red dots) of octanethiols bind to a sheet of gold atoms (yellow dots), and the octyl chains (black dots) form a monolayer. The second sulfur atom of a 1,8-octanedithiol molecule inserted into the monolayer binds to a gold nanoparticle, which in turn is contacted by the gold tip of the conducting AFM. (**B**) $I(V)$ curves measured with the apparatus diagrammed in (A). The five curves shown are representative of distinct families, $NI(V)$, that are integer multiples of a fundamental curve, $I(V)$ ($N$ = 1, 2, 3, 4, and 5). (**C**) Curves from (B) divided by 1, 2, 3, 4, and 5. (**D**) Histogram of values of a divisor, $X$ (a continuous parameter), chosen to minimize the variance between any one curve and the fundamental curve, $I(V)$. It is sharply peaked at integer values 1.00 $\pm$ 0.07 (1256 curves), 2.00 $\pm$ 0.14 (932 curves), 3.00 $\pm$ 0.10 (1002 curves), 4.00 $\pm$ 0.10 (396 curves) and 5.00 $\pm$ 0.13 (993 curves). (Spreads are $\pm$1 SD.) Of 4579 randomly chosen curves, over 25% correspond to the $X$ = 1 (single-molecule) peak. No obvious correlation was noted between particle size and number of molecules contacted. Conducting atomic force microscopy data were acquired with a PicoSPM microscope (Molecular Imaging) using silicon cantilevers (spring constant, 0.35 N/m) sputter-coated with 5 nm of chromium followed by 50 nm of gold. Imaging was done under toluene in a nitrogen atmosphere.

A key factor permitting identification of the fundamental curves in Fig. 1 is the lack of dependence on contact force for these chemically bonded contacts, as shown in Fig. 2B (dashed line). In contrast, nonbonded contacts made by moving the tip onto the alkanethiol monolayer (dotted line) show the strong force dependence previously reported (*3*, *10*, *11*). The stress on the monolayer is probably somewhat higher when contact is made through a gold nanoparticle rather than by direct contact with the AFM, because the particles are smaller than the end radius of the AFM probe (measured to be about 10 nm by scanning electron microscopy). Thus, the monolayer must undergo substantial deformation in both cases. The lack of force dependence of the chemically bonded contact implies that (i) interatomic distances within a molecule do not change much as the film is stressed, which is consistent with simulations of deformation in alkanethiol monolayers (*21*); and (ii) the bonds between the molecule and the metal do not change substantially either.

The physical structures of the monolayers investigated here were characterized by means of scanning tunneling microscopy. An image of the alkanethiol monolayer with inserted dithiol molecules (bright spots) is shown in Fig. 3A. It has been suggested that desorption of alkanethiols from a gold surface might occur via a disulfide (*22*). Although this process could lead to the insertion of a pair of octanedithiols, some of these molecules could in

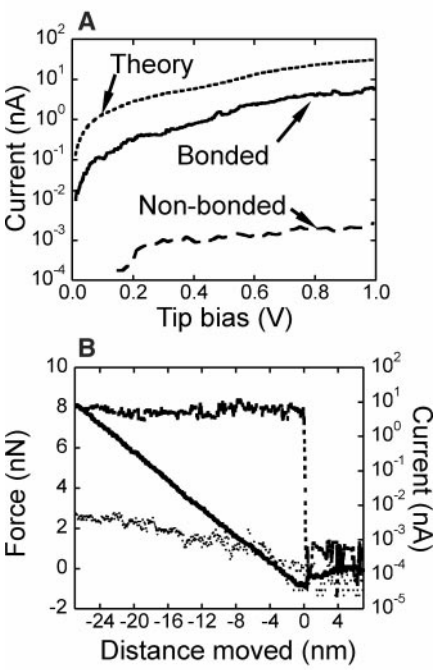


**Fig. 2.** (**A**) Current (on a log scale) as a function of voltage as calculated from first principles with no adjustable parameters (dashed line), as measured for a bonded single molecule (solid line), and for a nonbonded contact (contact force = 6 nN) to the surrounding octanethiol matrix (broken line) (noise-dominated data at low bias are suppressed). (**B**) Current and force measured as a conducting AFM cantilever (biased at +1 V) is moved toward the sample surface. Nominal contact is achieved at 0 distance, and negative values imply continued motion toward the Au(111) interface. When the probe approaches a gold nanoparticle, the current (dashed line) through the nanoparticle jumps to its final value on contact. When the surrounding octanethiol matrix is contacted, current (dots) is much smaller and depends on force (heavy solid line).

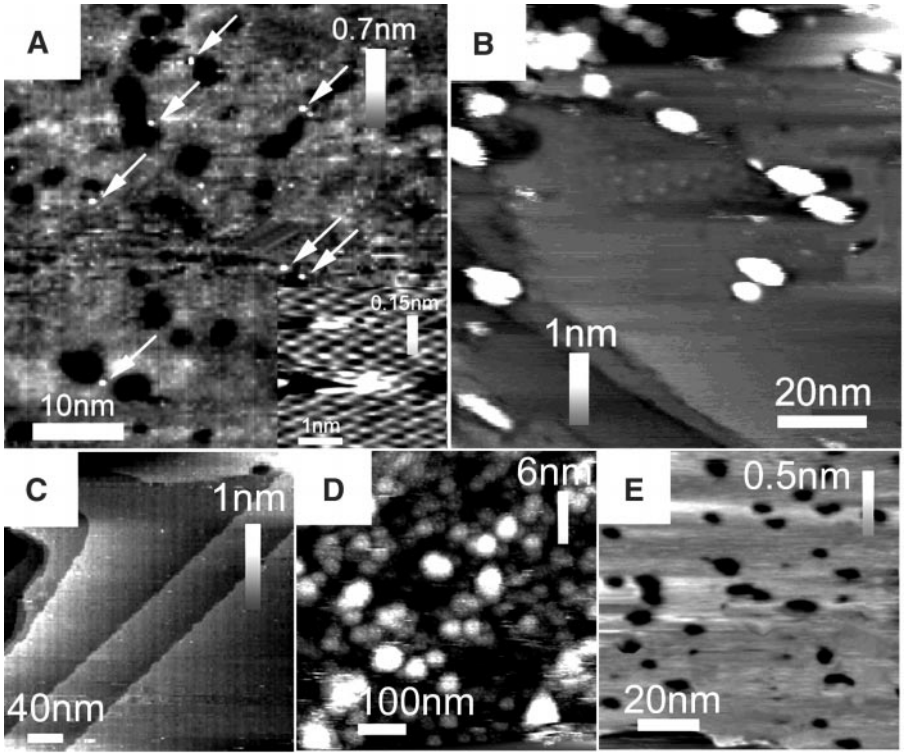


**Fig. 3.** STM images of (**A**) 1,8-octanedithiol molecules inserted into an octanethiol monolayer. Arrows point to the protruding thiols (shown at molecular resolution in the inset). The bright spots increase in density, but not in apparent size, with increasing dithiol exposure. (**B**) A mixed monolayer similar to that shown in (A) after incubation with gold nanoparticles that attached to the protruding thiols (the apparent diameter of the particles is increased owing to the finite size of the STM tip). The density of attached gold particles is of the same order of magnitude as the density of protruding thiols measured in (A). Controls are shown in (C) through (E). (**C**) Pure 1,8-octanedithiol monolayer. (**D**) The same monolayer after incubation with the gold nanoparticle suspension and rinsing, showing that the whole surface is covered with large gold aggregates. (**E**) A pure octanethiol monolayer subjected to the same treatment, showing that no gold particles are bound. All STM images were obtained with electrochemically etched PtIr tips using a PicoSPM with the sample under toluene and operating in a dry nitrogen environment.

turn desorb in pairwise fashion with an adjacent octanethiol, still leading to a (perhaps small) single-molecule "fundamental" peak shown in Fig. 1C. This possibility, coupled with the narrow peak widths and the population distribution (see legend to Fig. 3), render remote the possibility that the fundamental curve in Fig. 1 represents two molecules. After incubation with the suspension of gold nanoparticles, isolated conducting particles of gold attached to the monolayer were observed (Fig. 3B). Control experiments showed that a pure 1,8-octanedithiol monolayer (Fig. 3C) became covered by large gold aggregates when treated with the nanoparticle suspension (Fig. 3D), whereas the pure octanethiol monolayer was unaffected (Fig. 3E). Thus, the gold particles only attached to the inserted octanedithiol molecules in the mixed monolayer.

Our approach to measuring molecular conductivity avoids the effects of variations in contact force and other problems encountered with nonbonded contacts. Nonbonded molecular contacts are found to be highly resistive and to have $I(V)$ characteristics that are quite different from those of molecules with bonded contacts, showing that the nonbonded contact dominates electrical properties. In contrast, the bonded contacts are highly reproducible and lead to measurements that are in much better agreement with first-principles simulations without adjustable parameters. This approach is straightforward and easily applied to other types of molecules, opening a new avenue for exploring molecular electronics.

### References and Notes


1. M. A. Reed, C. Zhou, C. J. Muller, T. P. Burgin, J. M. Tour, *Science* **278**, 252 (1997).
2. S. Frank, P. Poncharal, Z. L. Wang, W. A. de Heer, *Science* **280**, 1744 (1998).
3. G. Leatherman *et al*., *J. Phys. Chem. B* **103**, 4066 (1999).
4. M. Dorogi, J. Gomez, R. Osifchin, R. P. A. Andres, *Phys. Rev. B* **52**, 9071 (1995).
5. D. I. Gittins, D. Bethell, D. J. Schiffrin, R. J. Nichols, *Nature* **408**, 67 (2000).
6. R. Holmlin *et al*., *J. Am. Chem. Soc.* **123**, 5075 (2001).
7. H. W. Fink, C. Schoenberger, *Nature* **398**, 407 (1999).
8. D. Porath, A. Bezryadin, S. de Vries, C. Dekkar, *Nature* **403**, 635 (2000).
9. S. Datta, W. Tian, *Phys. Rev. Lett.* **79**, 2530 (1997).
10. D. J. Wold, C. D. Frisbie, *J. Am. Chem. Soc.* **123**, 5549 (2001).
11. K. A. Son, H. I. Kim, J. E. Houston, *Phys. Rev. Lett.*, **86**, 5357 (2001).
12. M. DiVentra, S. T. Pantelides, N. D. Lang, *Phys. Rev. Lett.* **84**, 979 (2000).
13. M. T. Cygan *et al*., *J. Am. Chem. Soc.* **120**, 2721 (1998).
14. Pure octanethiol monolayers and 1,8-octanedithiol monolayers (*15*) were formed from 1 mM solutions in toluene left in contact with flame-annealed Au(111) (*16*) overnight. Mixed monolayers were formed by overnight incubation of octanethiol monolayers on Au(111) in a 1 mM solution of 1,8-octanedithiol in toluene. Freshly prepared gold nanoparticles of core diameter less than 2 nm (*17*) were suspended to a concentration of 0.25 g/liter in methylene chloride and incubated with the mixed monolayers overnight. The resulting films were rinsed in dichloromethane, then toluene, and were subsequently imaged in toluene. Isolated conducting particles of gold attached to the monolayer were observed and used as contact points for a freshly prepared gold-coated AFM probe.
15. J. S. Yang, *et al*., *J. Org. Chem.* **65**, 871 (2000).
16. J. A. DeRose, T. Thundat, L. A. Nagahara, S. M. Lindsay, *Surf. Sci.* **256**, 102 (1991).
17. W. W. Weare, S. M. Reed, M. G. Warner, J. E. Huchison, *J. Am. Chem. Soc.* **122**, 12890 (2000).
18. The calculation followed Mujica *et al*. (*19*) using

Green's function elements obtained from Fireballs-96 (*20*). This is a pseudopotential density functional technique, implemented here with a minimal numerical basis for H, C, and S, and an $sp^3d^5$ basis for Au. The molecular structure was first optimized with Hellmann-Feynman forces, with the molecule embedded in an infinite octanedithiol matrix between two gold slabs. The two-dimensional unit cell consisted of an octanedithiol molecule connected at each end to a 2 × 2 Au surface. The terminal H was removed from each thiol group, and the sulfur atoms were found to bind to the gold about 0.194 nm above the surface and equidistant from three Au surface atoms. The current was calculated for this geometric structure by contacting a single molecule between a pair of Au(111) clusters four by four by five atoms deep (avoiding technical problems for current calculations in an infinite system). A similar process was used for the nonbonded structure.

19. V. Mujica, M. Kemp, M. A. Ratner, *J. Chem. Phys.* **101**, 6849 (1994).
20. A. A. Demkov, J. Ortega, O. F. Sankey, M. P. Grumbach, *Phys. Rev.* **B52**, 1618 (1995).
21. J. I. Siepmann, I. R. McDonald, *Phys. Rev. Lett.* **70**, 453 (1993).
22. J. B. Schlenhoff, M. Li, H. Ly, *J. Am. Chem. Soc.* **117**, 12528 (1995).
23. We thank L. Nagahara (Motorola Labs) and G. Ramachandran (Arizona State University) for useful discussions. Supported by NSF.

12 July 2001; accepted 27 August 2001

# Present-Day Crustal Deformation in China Constrained by Global Positioning System Measurements

**Qi Wang,[1] Pei-Zhen Zhang,[2]* Jeffrey T. Freymueller,[3] Roger Bilham,[4] Kristine M. Larson,[5] Xi'an Lai,[1] Xinzhao You,[1] Zhijun Niu,[2] Jianchun Wu,[2] Yanxin Li,[6] Jingnan Liu,[7] Zhiqiang Yang,[8] Qizhi Chen[3]**

**Global Positioning System (GPS) measurements in China indicate that crustal shortening accommodates most of India's penetration into Eurasia. Deformation within the Tibetan Plateau and its margins, the Himalaya, the Altyn Tagh, and the Qilian Shan, absorbs more than 90% of the relative motion between the Indian and Eurasian plates. Internal shortening of the Tibetan plateau itself accounts for more than one-third of the total convergence. However, the Tibetan plateau south of the Kunlun and Ganzi-Mani faults is moving eastward relative to both India and Eurasia. This movement is accommodated through rotation of material around the eastern Syntaxis. The North China and South China blocks, east of the Tibetan Plateau, move coherently east-southeastward at rates of 2 to 8 millimeters per year and 6 to 11 millimeters per year, respectively, with respect to the stable Eurasia.**

Asia is a modern example of large-scale continental deformation (Fig. 1) and an ideal natural laboratory for its studies. Unfortunately, much of the region is remote, and thus the kinematics of Asia has been, until recently, poorly understood. Although much of its late Cenozoic deformation is explained by the collision and subsequent penetration of India into Eurasia (*1*), how Eurasia deforms in response to the collision is still subject to debate (*2, 3*), and a complete kinematic description of deformation over the entire region has not been available. Existing kinematic models (*4, 5*) rely on sparse data sets that can only describe the complex deformation of Eurasia on length scales of 200 km or larger, and lack data from critical regions. We present a synthesis of GPS velocities in China and its vicinity that provides new insights into the kinematics of Eurasia.

Much of the actively deforming part of Eurasia lies within China, including the Tibetan plateau, and parts of the Himalaya, Tian Shan, and Pamir mountain ranges (Fig. 1). Since the early 1990s, several regional GPS networks for active tectonic studies were established in China and neighboring regions (*6–15*). These networks were surveyed in campaign mode, usually at 1- to 2-year intervals. Each individual network was originally designed to address local problems, and it has been difficult to merge the data together, due to different data analysis strategies. We obtain a self-consistent velocity field by analyzing the original raw data from several different regional networks and merging them into a self-consistent solution.

We combined original data from GPS campaigns carried out between 1991 and 2001 by 10 Chinese and U.S. agencies or universities (*16*). The regional GPS data were combined with continuous tracking data from a well-distributed set of global International GPS Service (IGS) stations using the GIPSY software (*17*). For data observed between 1991 and 1995, we used a global solution strategy in which parameters associated with GPS satellite orbits were estimated together with all station coordinates (*18*). A projection operator was applied to the covariance matrix to remove the components of the covariance matrix that are purely due to reference frame uncertainty (*19*). For data observed after 1995, a regional solution strategy was adopted, using fixed orbits and satellite clocks provided by NASA's Jet Propulsion Laboratory (*20*). A subset of IGS stations was used in the regional solutions (*21*). Next, the daily free network solutions were each transformed into the ITRF97 (International Terrestrial Reference Frame, epoch 1997.0) by estimating a seven-parameter similarity transformation for each (*22*). We estimated the transformation for each day, on the basis of the common stations that are present both in ITRF97 and in the daily solution, and weighted each station by their respective uncertainties. The 1250 daily solutions were used as data to determine the station velocities and station coordinates at epoch 1995.0 by a standard weighted least-squares adjustment (*23*). The velocities in ITRF97 were then transformed into velocities in a Eurasia-fixed reference frame (*24*). The aggregate velocity solution of 354 stations (*25*) provides an image, to date, of present-day crustal deformation in Asia (Fig. 2). The velocity solutions in both ITRF97 and Eurasia-fixed frames are available at *Science*'s Web site (*26*). Most velocity uncertainties, propagated by the errors of Eurasia rotation parameters, are in the range of 1 to 4 mm/year, except some stations with an observation interval shorter than 1.5 years. The mean uncertainties in northward velocities relative to Eurasia are 2.2 mm/year and 2.4 mm/year for eastward components.

Stations located on the northern Ganges plains, south of the Himalaya, show northward movement (N19°-22°E) at a rate of 36 to 38 mm/year with respect to stable Eurasia (*27*), consistent with some previous studies (*5, 13, 28*). Bangalore (station IISC) in southern India has a velocity of 35.9 ± 1.0 mm/year in the direction of N26.9° ± 1.7°E. The

[1]Institute of Seismology, China Seismological Bureau, Wuhan 430071, China. [2]Center for Crustal Movement Studies and Institute of Geology, China Seismological Bureau, Beijing 100029, China. [3]Geophysical Institute, University of Alaska, Fairbanks, AK 99775, USA. [4]Department of Geological Sciences and CIRES, University of Colorado, Boulder, CO 80309, USA. [5]Department of Aerospace Engineering Sciences, University of Colorado, Boulder, CO 80309, USA. [6]First Crustal Deformation Monitoring Center, China Seismological Bureau, Tianjin 300180, China. [7]School of Geodesy and Geomatics, Wuhan University, Wuhan, 430071, China. [8]Department of Surveying Engineering, Chang'an University, Xi'an 710064, China.

*To whom correspondence should be addressed. E-mail: peizhen@public3.bta.net.cn.